ADVANCED MATERIALS

Supporting Information

for *Adv. Mater.,* DOI: 10.1002/adma.202102691

3D Temporary-Magnetized Soft Robotic Structures for Enhanced Energy Harvesting

Liming Miao, Yu Song, Zhongyang Ren, Chen Xu, Ji Wan, Haobin Wang, Hang Guo, Zehua Xiang, Mengdi Han, and Haixia Zhang**

Three-dimensional temporary-magnetized soft robotic structures for enhanced energy harvesting

Liming Miao,[1] Yu Song,[1] Zhongyang Ren, Chen Xu, Ji Wan, Haobin Wang, Hang Guo, Zehua Xiang, Mengdi Han,* and Haixia Zhang*

Liming Miao, Yu Song, Zhongyang Ren, Ji Wan, Haobin Wang, Zehua Xiang and Haixia Zhang
National Key Lab of Nano/Micro Fabrication Technology, Institute of Microelectronics, Peking University, Beijing, 100871, China

Yu Song
Department of Medical Engineering, Division of Engineering and Applied Science, California Institute of Technology, Pasadena, California, 91125, USA.

Chen Xu, Hang Guo and Haixia Zhang
Academy for Advanced Interdisciplinary Studies, Peking University, Beijing, 100871, China

Mengdi Han
Department of Biomedical Engineering, College of Future Technology, Peking University, Beijing, 100871, China.

[1]These authors contribute equally.

*email: hmd@pku.edu.cn; hxzhang@pku.edu.cn

Supplementary Materials

Note S1. Deformation of 2D PNC film under the magnetic field of a magnet

According the **Refs. S1,2**, the magnetic potential energy ($W^{magnetic}$) can be simplified as:

$$W^{magnetic} = -\frac{1}{\mu_0} M^{magnetized}(x,y) \cdot H^{applied}(x,y) \tag{S1}$$

Assume that the induced magnetic field is linearly proportional to the external magnetic field when the external magnetic field is between 0 and 0.3 T. The magnetization of PNC film ($M^{magnetized}$) and magnetic field of the magnet (H^{magnet}) can be derived as:

$$M^{magnetized} = \chi \cdot H^{magnet} \tag{S2}$$

$$H^{magnet} = \frac{1}{\mu_0} \cdot B^{applied} \tag{S3}$$

Then the volume magnetic force can be derived as:

$$F^{magnetic} = -\nabla W^{magnetic} = \frac{\chi}{\mu_0^2} \cdot \nabla B^{applied^2} \tag{S4}$$

, where μ_0, $B^{applied}$ and $F^{magnetic}$ denote vacuum permeability, applied magnetic field, and magnetic force per volume from the magnet, respectively.

According to the distribution of the magnetic field from the magnet, we simplify the model of 2D PNC film with two regions: strong magnetized region (B_S) and weak magnetized region (B_W) (**Figure S10**, Supporting Information). Because of the short-distance action of the magnet, we assume that both regions are magnetized with uniform loads.

For the 2D PNC film with the thickness (D), length (L), and width (w), the point load (Q) can be described as:

$$Q = \frac{wD\chi}{\mu_0^2} \cdot \left| B^{applied} \right|^2 = \frac{wD}{\mu_0} \cdot \left| M^{magnetized} \right| \cdot \left| B^{applied} \right| \tag{S5}$$

The maximum movement (S) of the 2D PNC film under the magnetic field can be described as:

$$S = S_1 + S_2 = \frac{QL_S^3}{3EI} + \frac{QL_W^3}{3EI} \propto \frac{\chi}{\mu_0^2 GD^2} (B_S^2 L_S^3 + B_W^2 L_W^3) \tag{S6}$$

, where E is the elastic modulus and G is the shear modulus of PNC film ($G = 3E$), respectively. I is area moment of inertia, defined as $I = WD^3/12$. Considering that the 2D PNC film is always at millimeter or centimeter scales while the magnet is with millimeter diameter, the scale effect is much smaller that the magnetization effect:

$$\frac{L_W^3}{L_S^3} \ll \frac{B_S^2}{B_W^2} \tag{S7}$$

$$B_S^2 L_S^3 + B_W^2 L_W^3 \approx B_S^2 L_S^3 \tag{S8}$$

, then the movement can be further simplified as:

$$S \propto \frac{\chi B_S^2 L_S^3}{\mu_0^2 G D^2} \propto \frac{\left| M^{magnetized} \right|}{G D^2} \tag{S9}$$

Under the certain condition, S is closely related to the $M^{magnetized}$, G and D of 2D PNC film.

Both $M^{magnetized}$ and G are dependent on the mass ratio of NdFeB microparticles, and the thickness of 2D PNC film determines both M and D^2. Therefore, to realize the maximum S with great magnetic-controlled performance, it is essential to adopt optimal 2D PNC film with high M/G and M/D^2.

References

S1. Kim, Y., Parada1, G., Liu, S. & Zhao, X. Ferromagnetic soft continuum robots. *Sci. Robot.* **2019**, *4*, eaax7329.

S2. Zhao, R., Kim, Y., Chester, S., Sharma, P., Zhao, X. Mechanics of hard-magnetic soft materials. *J. Mech. Phys. Solids* **2019**, *124*, 244.

Note S2. Working mechanism for the organic solar cells

The detailed working mechanism of the organic solar cells (OSC) with the generation, transmission, and collection of internal charge to produce electrical signals can be divided into the following steps (**Figure 5b**).

1. First, the photovoltaic material of the OSC active layer absorbs photos to generate excitons.

2. Second, excitons diffuse to the interface of the donor ($PC_{60}BM$) and the receptor (P3HT). Considering that excitons are highly susceptible to recombination during the diffusion process, it is feasible to reduce the diffusion time of excitons to the donor and acceptor interfaces through the decrease of thickness of the active layer. However, thin structure inevitably weakens the capability to absorb light. Then we adopt a trap structure to increase the amount of light radiation on the active layer, to improve the photoelectric conversion performance of OSC.

3. Third, the excitons at the donor and acceptor interfaces dissociate into electrons and holes. Electrons enter the acceptor lowest-unoccupied-molecular-orbital (LUMO) level and holes enter the highest-occupied-molecular-orbital (HOMO) level of the donor, respectively.

4. Next, the separated holes are transported to the anode along the channel formed by the donor material, and the electrons are transported to the cathode along the channel formed by the acceptor material.

5. Finally, holes and electrons are collected by the anode and cathode to form a photocurrent.

According to the photovoltaic effect, the photocurrent (I_φ) can be described as:

$$I_\varphi = \frac{\eta q}{h\nu}(1-e^{-\alpha d})\varphi_{e,\lambda} \tag{S10}$$

, where h is the Planck's constant, ν is the frequency of the light, η is the photoelectric conversion efficiency of the photovoltaic material, α is the absorption coefficient of the material to light, and $\varphi_{e,\lambda}$ is the incident light radiant flux, which is influenced by the incident angle of external light. It can be clearly seen that the I_φ is closely related to the $\varphi_{e,\lambda}$ in a certain environment. Therefore, the development of real-time solar tracking system provides a feasible approach to enhance the energy harvesting and photoelectric conversion efficiency of OSC by precise adjustment of incident angle.

Supplementary Figures

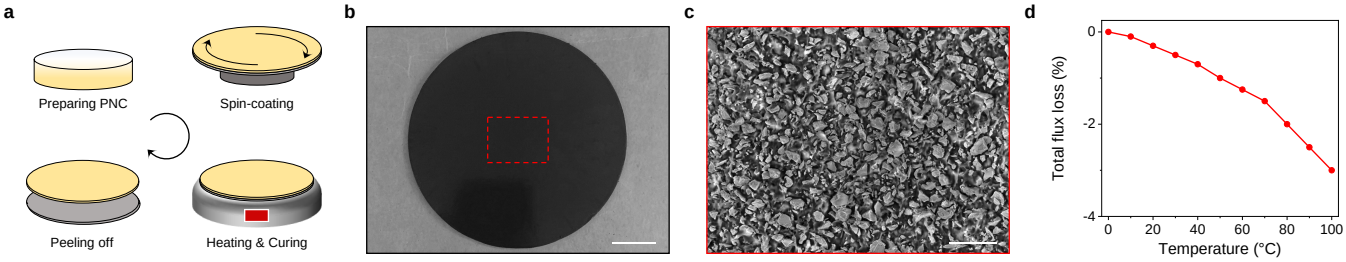

Figure S1. Preparation of the 2D PNC film. a) Fabrication process of the 2D PNC film. **b**) Optical image of the prepared 2D PNC film. Scale bar 2 cm. **c**) SEM image of the PNC film. Scale bar, 25 μm. **d**) Effect of temperature on total flux loss of NdFeB microparticles.

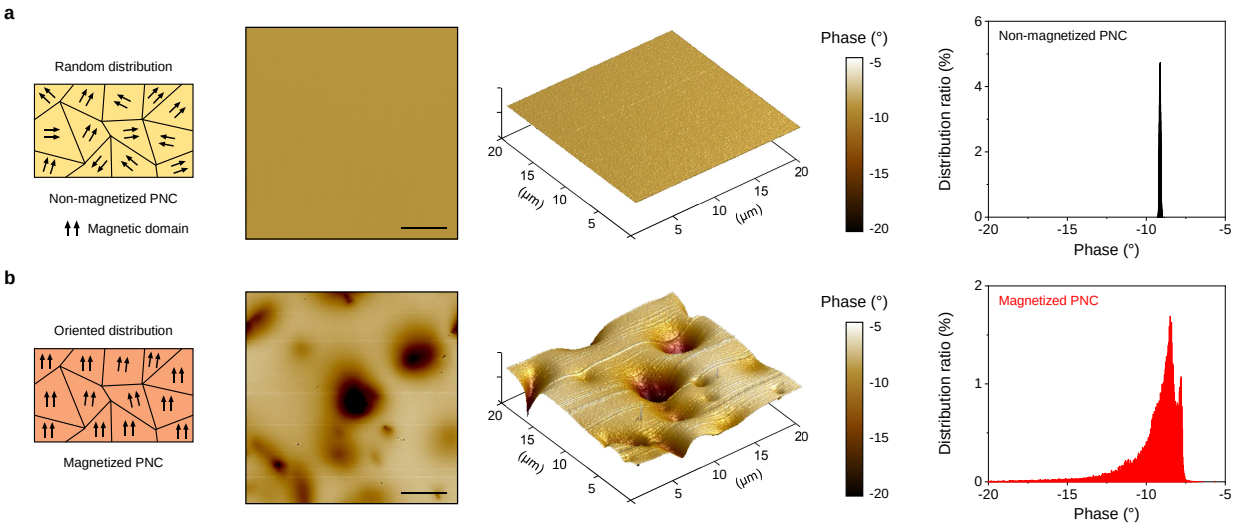

Figure S2. AFM characterization of the PNC film with random and oriented distribution of magnetic domains. a) Schematic, 2D and 3D AFM images, and phase distribution of magnetic domains of the non-magnetized PNC film. Scale bar, 4 μm. **b**) Schematic, 2D and 3D AFM images, and phase distribution of magnetic domains of the magnetized PNC film. Scale bar, 4 μm.

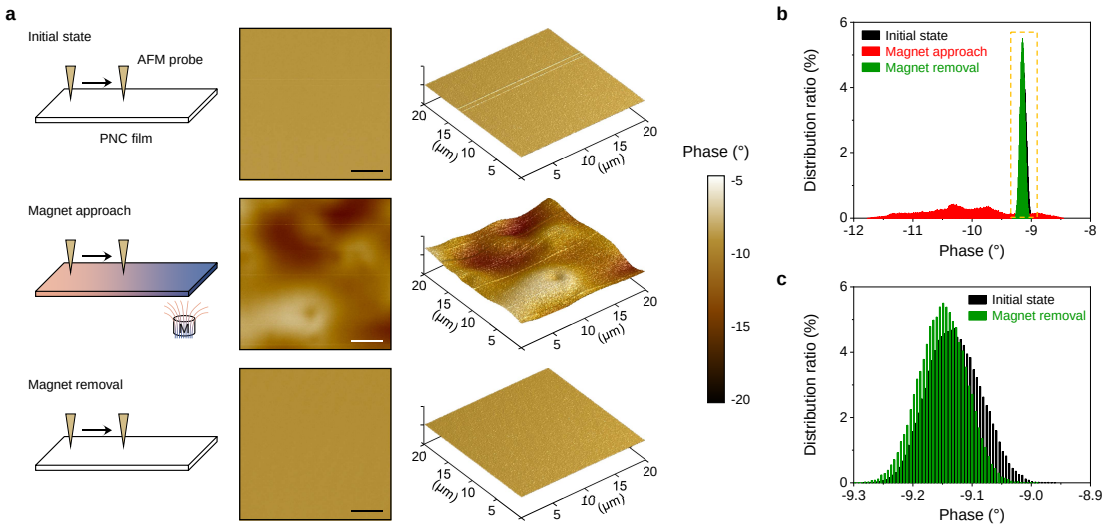

Figure S3. AFM characterization of the PNC film with temporary-magnetized process. a) Schematic, 2D and 3D AFM images of magnetic domains in the PNC film during the approach and removal of the external magnet. Scale bars, 4 μm. **b**) Phase distribution of magnetic domains in the PNC film in different states. **c**) Enlarged phase distribution of magnetic domains in the PNC film in initial state and after the removal of the magnet.

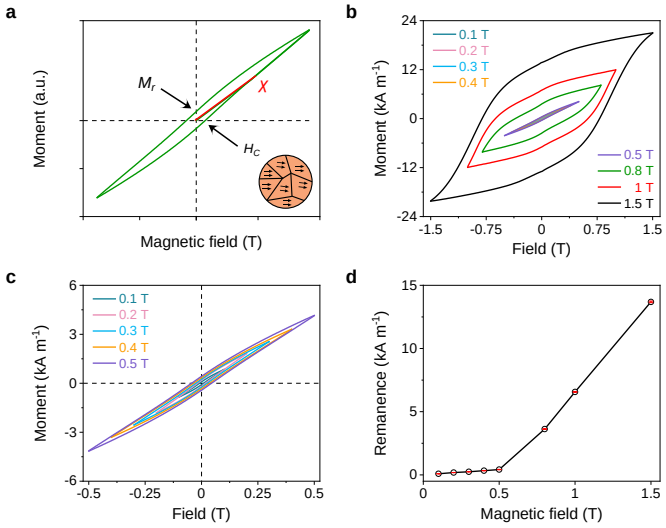

Figure S4. Static magnetic hysteresis loops of the PNC film under different magnetic fields. **a**) Magnetization curve of the PNC film under a small magnetic field. **b**,**c**) Static magnetic hysteresis loops of the PNC film under different magnetic fields, **b**) from 0.1 T to 1.5 T, and **c**) from 0.1 T to 0.5 T. **d**) The remanence of the PNC film under different magnetic fields.

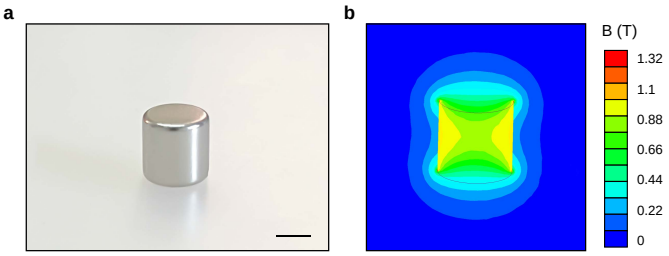

Figure S5. The magnetic field analysis of a magnet. a) Optical image of a commercial hard magnet. Scale bar, 2 mm. **b**) FEA result of the surface magnetic field of a magnet.

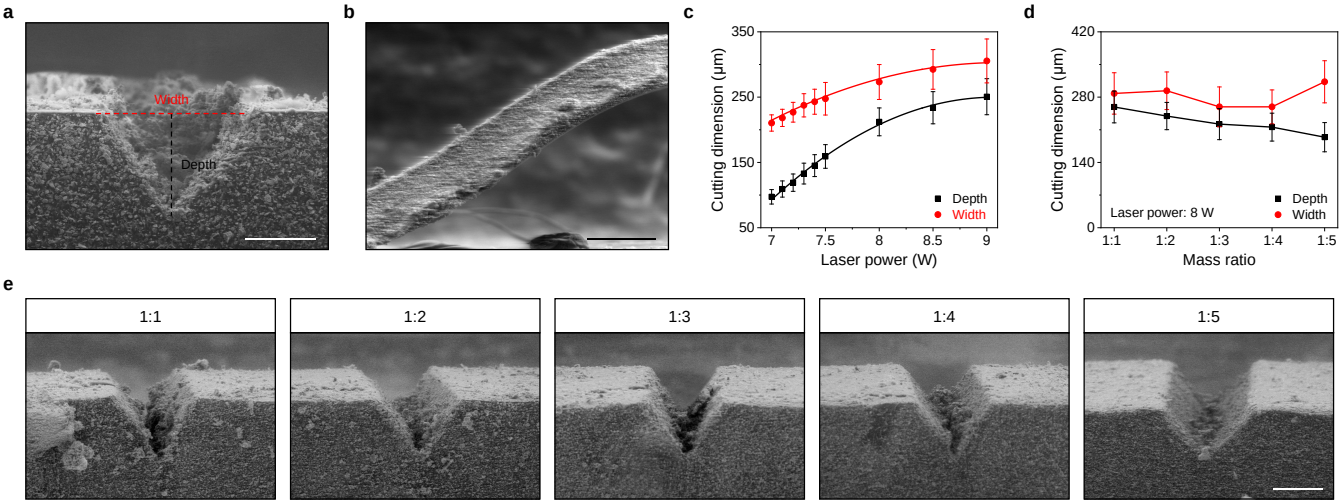

Figure S6. Effect of laser parameters and the mass ratio of NdFeB microparticles on the laser-patterning process. a,**b**) SEM images (cross section view) of **a**) the laser-cutting notch on PNC film and **b**) the patterned PNC film. Scale bars, 100 μm. **c**,**d**) Effects of **c**) the laser power and **d**) the mass ratio of NdFeB microparticles on the cutting depth and width. **e**) Cross-sectional SEM images of the laser-cutting notch on PNC film with different mass ratios of NdFeB microparticles. Scale bar, 200 μm.

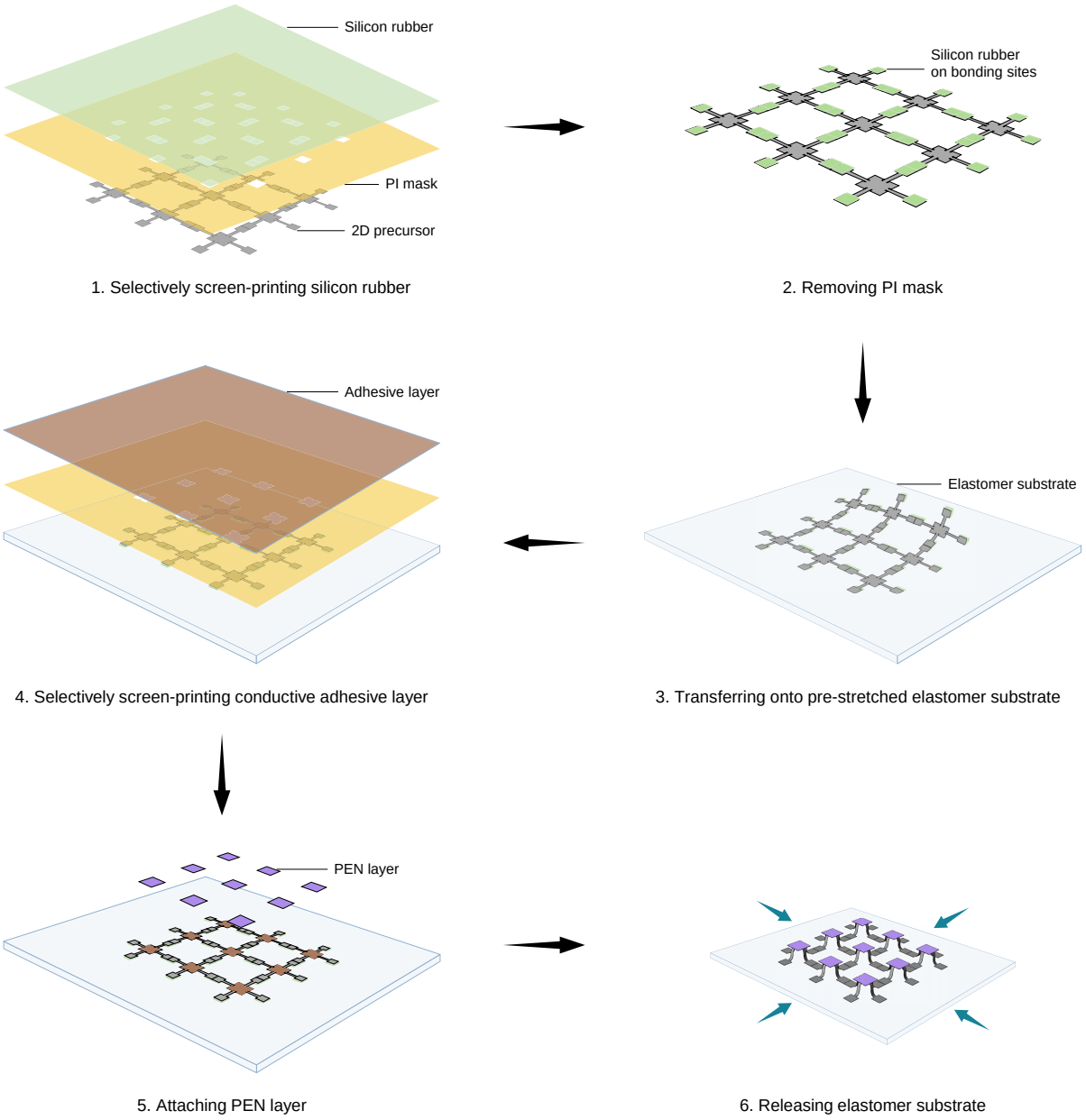

Figure S7. Schematic illustration of the mechanical-guided compressive-bulking process for 3D robotic structures.

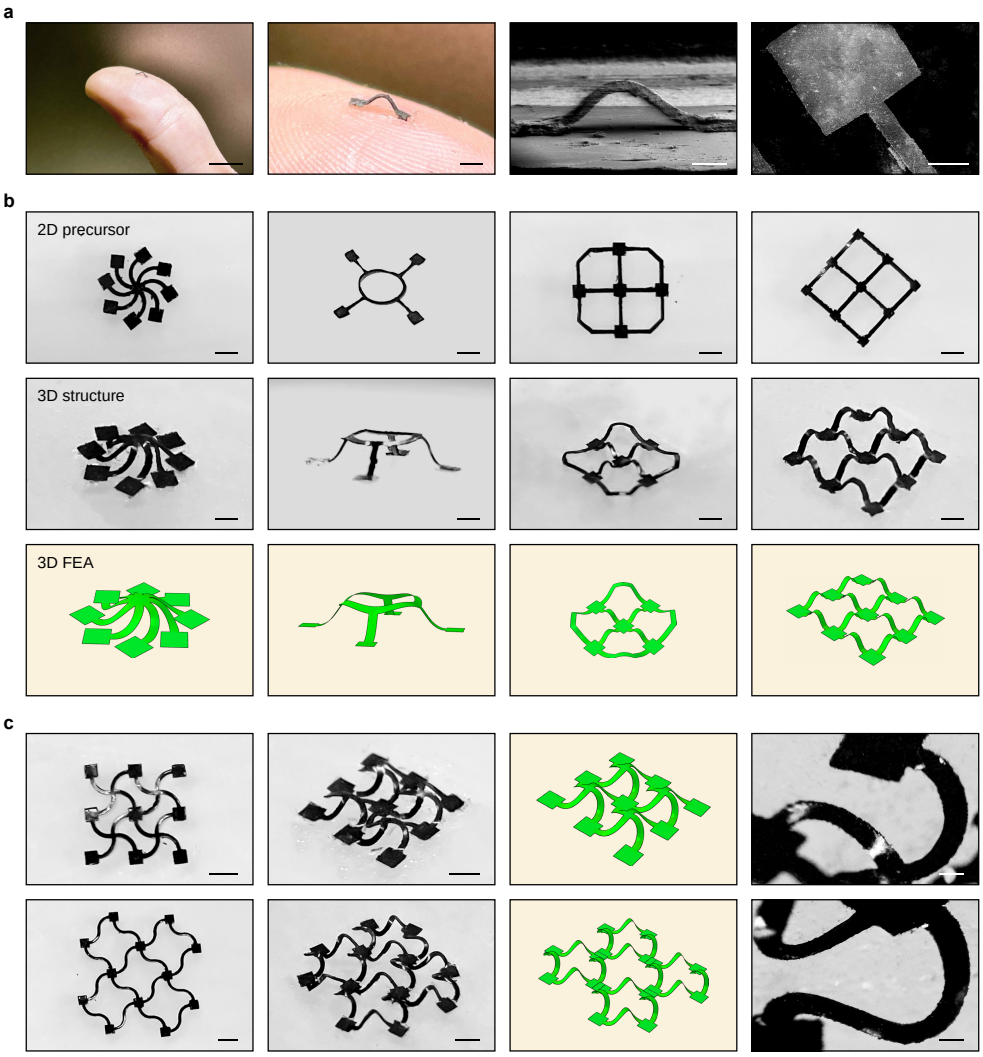

Figure S8. 3D robotic structures at different scales. a) Optical and SEM images of meso-scale 3D ribbon. Scale bars, 1 cm, 2 mm, 500 μm, and 500 μm, from left to right. **b**) Optical images of 2D precursors, 3D structures, and FEA predictions of sub-millimeter-scale 3D designs. Scale bars, 2 mm. **c**) Optical images of 2D precursors, 3D structures, FEA predictions, and enlarged optical images of millimeter-scale 3D designs. Scale bars, 2 mm for the left two columns, 500 μm for the right column.

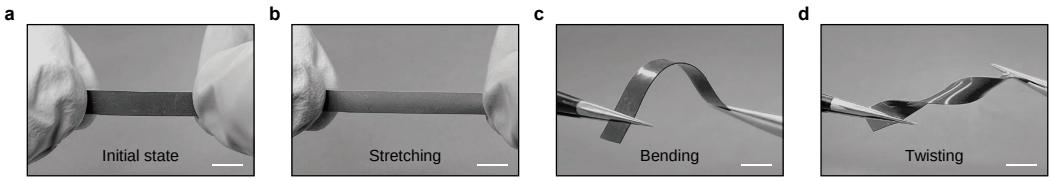

Figure S9. Mechanical properties of the prepared 2D PNC film. a-d) Optical images of PNC film under **a**) initial, **b**) stretching, **c**) bending, and **d**) twisting states. Scale bars, 5 mm.

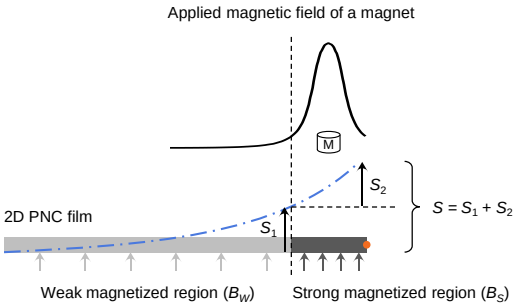

Figure S10. Schematic illustration of the movement of 2D PNC film under the magnetic field of a magnet with strong magnetized region, and weak magnetized region.

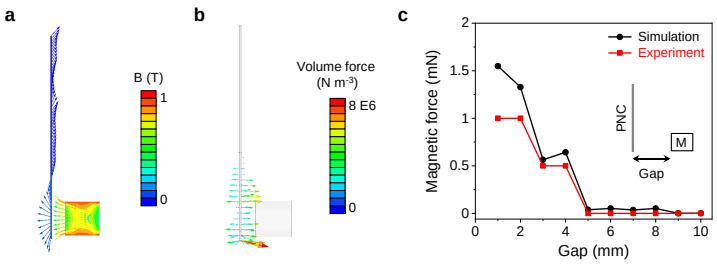

Figure S11. Magnetic force analysis for 2D PNC film. a,**b**) FEA results of **a**) the induced magnetic field and **b**) the magnetic force distribution of the PNC film. **c**) FEA and experimental results for the variation of magnetic force and gap between the 2D PNC film and the magnet.

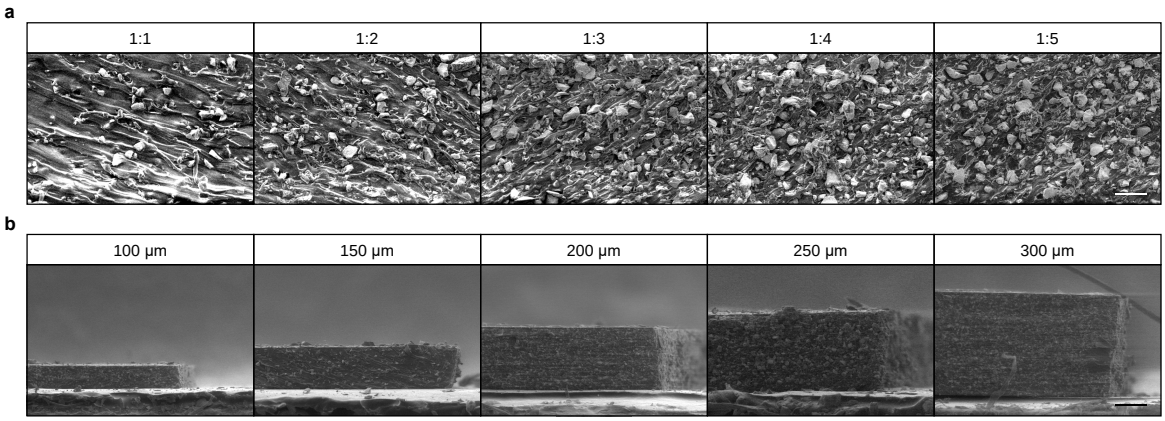

Figure S12. Surface morphologies of 2D PNC films with different parameters. a) SEM images of 2D PNC films with different mass ratios of NdFeB microparticles. Scale bar, 20 μm. **b**) SEM images of 2D PNC films with different thicknesses. Scale bar, 100 μm.

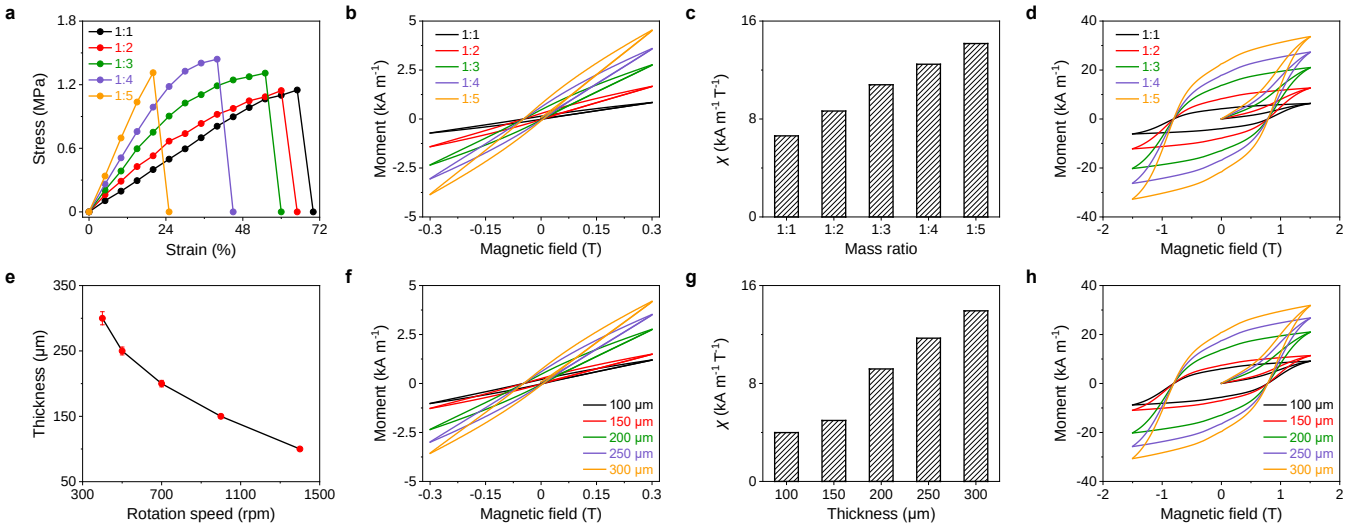

Figure S13. Evaluation of PNC films with different parameters. a) Strain-stress curves of PNC films with different mass ratios of NdFeB microparticles. **b-d**) Static **b**) magnetic hysteresis loops, **c**) corresponding susceptibility under the magnetic field of 0.3 T, and **d**) Static magnetic hysteresis loops under the saturated magnetic field of 1.5 T of PNC films with different mass ratios of NdFeB microparticles. **e**) Relationship between the thickness of PNC film and rotation speed. Error bars are the standard error deviation from three measurements. **f-h**) Static **f**) magnetic hysteresis loops, **g**) corresponding susceptibility under the magnetic field of 0.3 T, and **h**) the static magnetic hysteresis loops under the saturated magnetic field of 1.5 T of PNC films with different thicknesses.

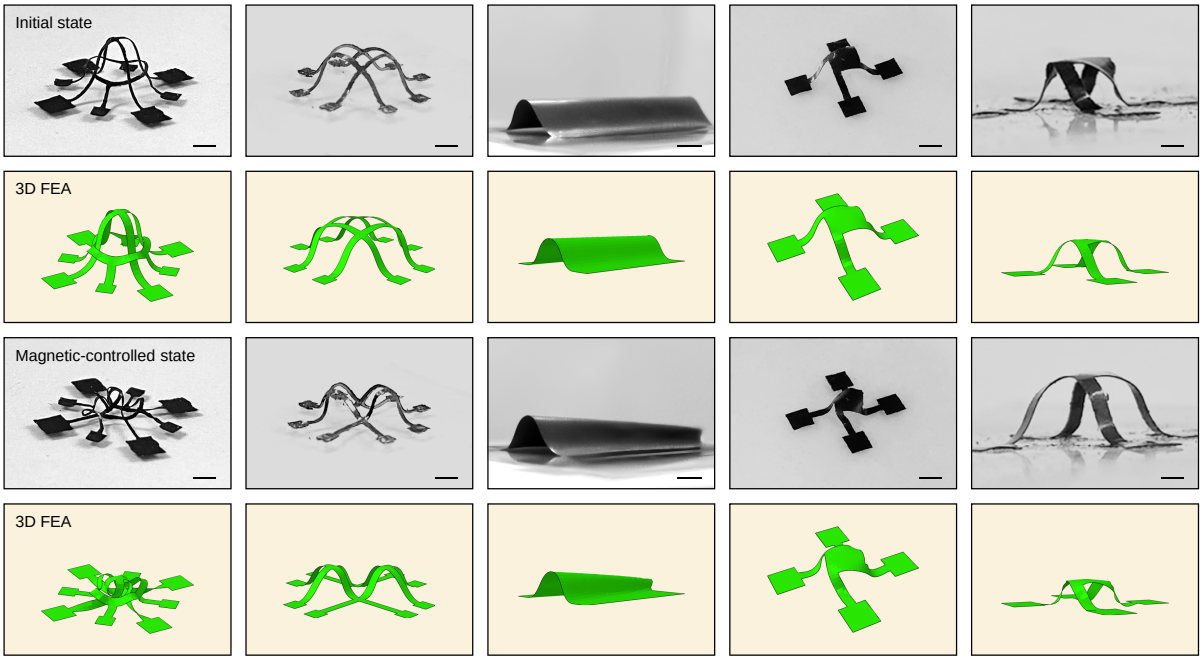

Figure S14. Optical images and FEA predictions of 3D robotic structures under the initial state and magnetic-controlled state. Scale bars, 5 mm.

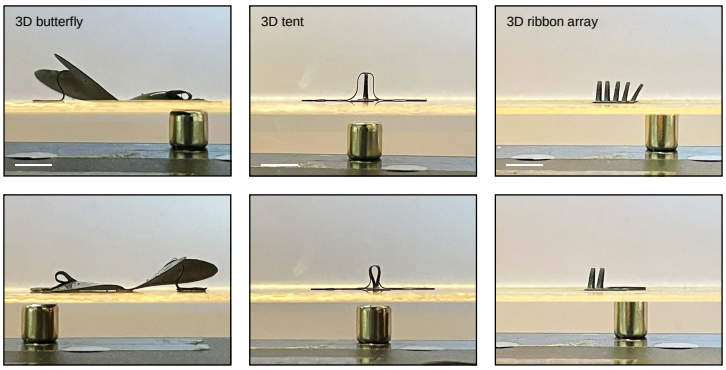

Figure S15. Optical images of detailed configuration of magnetic-controlled process of 3D robotic structures with the external magnet. Scale bars, 3 mm.

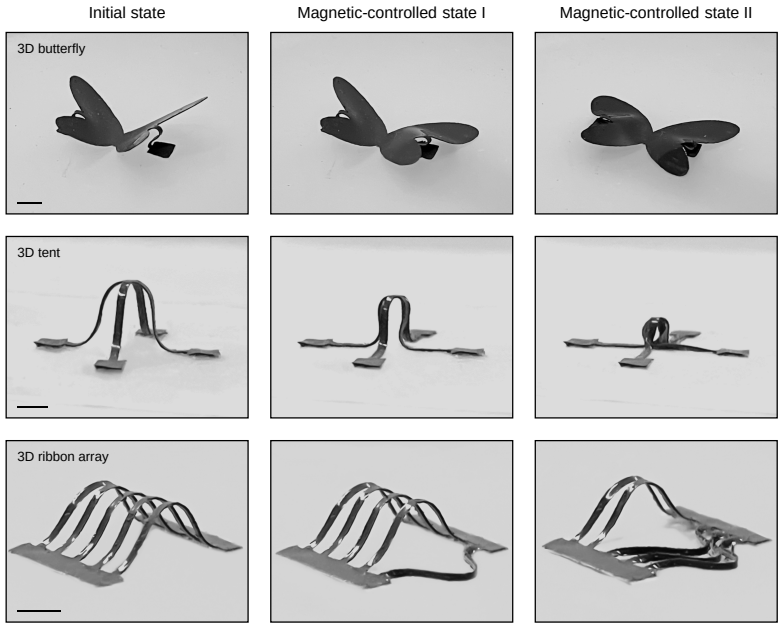

Figure S16. Optical images of different Fe-PDMS-based 3D robotic structures under initial and magnetic-controlled states. Scale bars, 2 mm.

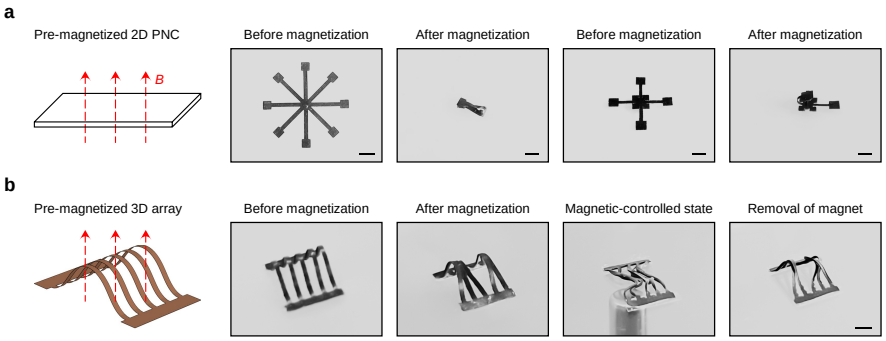

Figure S17. Schematic illustration and optical images of different 2D precursors and 3D robotic structures with pre-magnetized process. a) Patterned 2D precursors. Scale bars, 4 mm. **b**) 3D ribbon array. Scale bar, 2 mm.

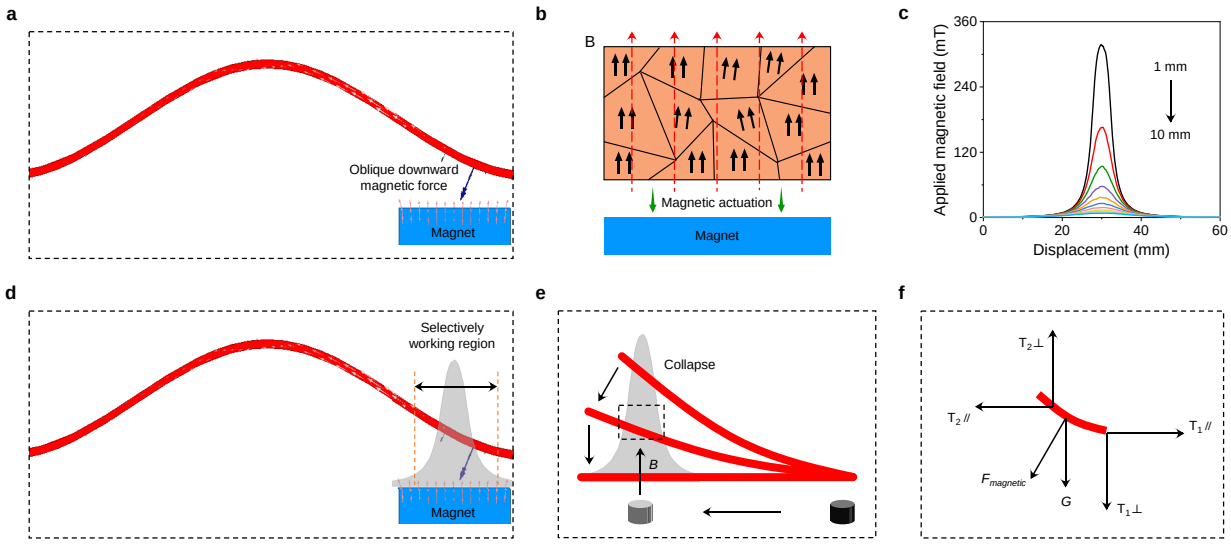

Figure S18. FEA results of the magnetic-controlled 3D ribbon. a) FEA results of volume force distribution on the 3D ribbon by the magnet. **b**) Schematic illustration of magnetic actuation. **c**) FEA results of applied magnetic fields of the magnet with different working gaps. **d**,**e**) Schematic illustration of **d**) the selectively working region of the 3D ribbon and **e**) the local deformation of the 3D ribbon. The gray area represents the surface magnetic field of the magnet. **f**) Force analysis of a unit of the magnetic-controlled 3D ribbon.

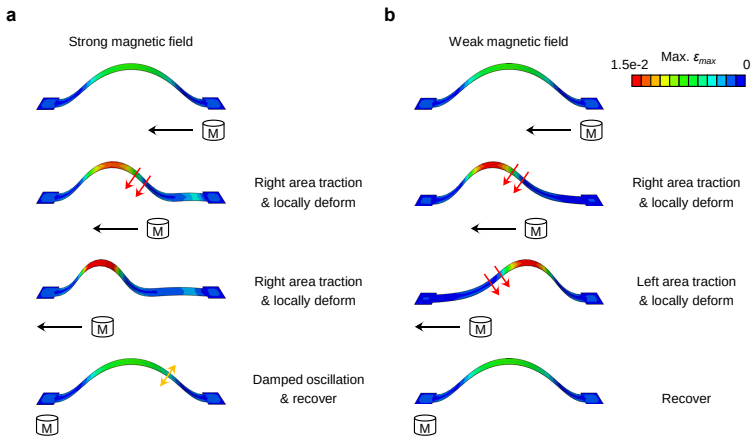

Figure S19. FEA results of the deformation of the 3D ribbon under different magnetic fields. **a**,**b**) The deformation process during the magnet movement under **a**) strong magnetic field (B > 0.15 T) and **b**) weak magnetic field (B < 0.15 T).

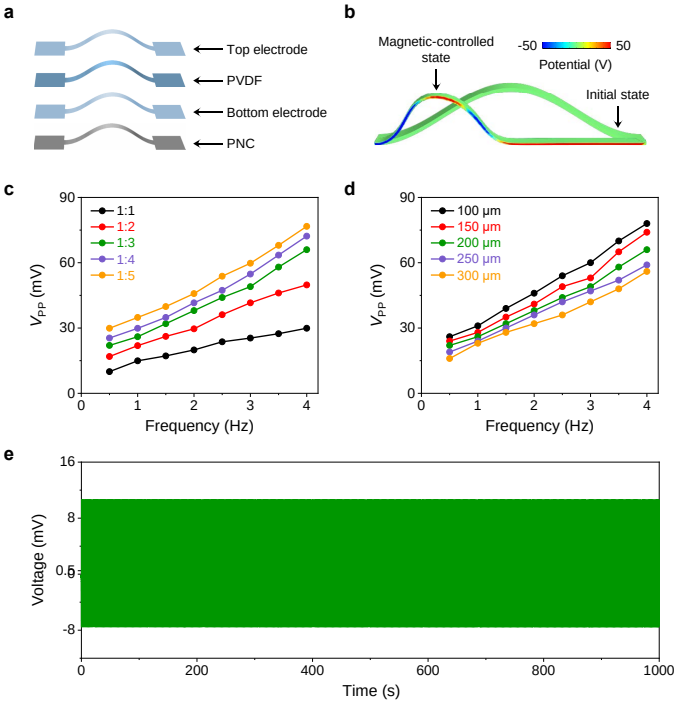

Figure S20. Characterization of the 3D piezoelectric ribbon. a) Exploded schematic illustration of the 3D piezoelectric ribbon. **b**) Simulated potential distribution of the 3D piezoelectric ribbon under the magnetic-controlled state. **c**,**d**) Frequency-domain peak-to-peak(V_{PP}) of the 3D piezoelectric ribbon with **c**) different mass ratios of NdFeB microparticles and **d**) different thicknesses. **e**) Long-term output stability of the 3D piezoelectric ribbon at the operating frequency of 1 Hz.

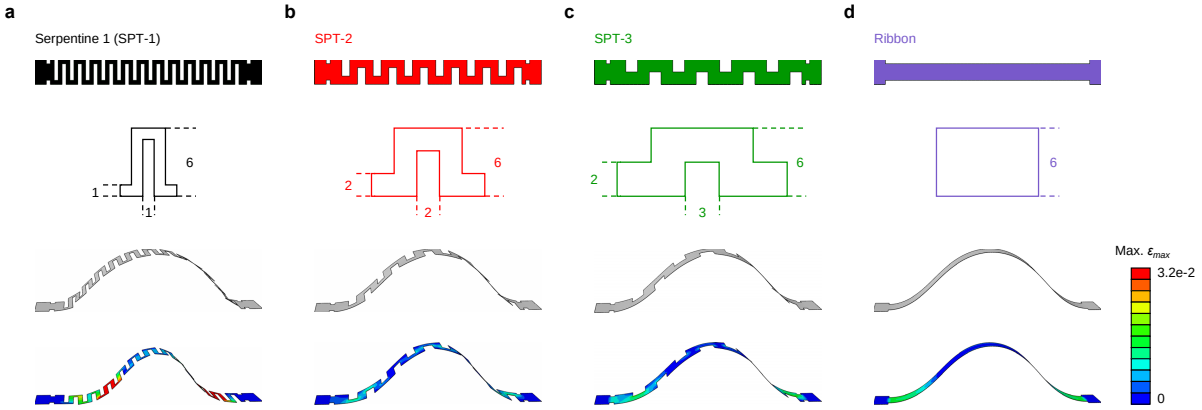

Figure S21. Schematic illustration of various 3D piezoelectric structures. a-d) Structural design, dimension parameters (unit: mm), and FEA results of strain distribution under initial state and magnetic-controlled state of **a**) serpentine-1 (SPT-1), **b**) SPT-2, **c**) SPT-3, and **d**) ribbon structure.

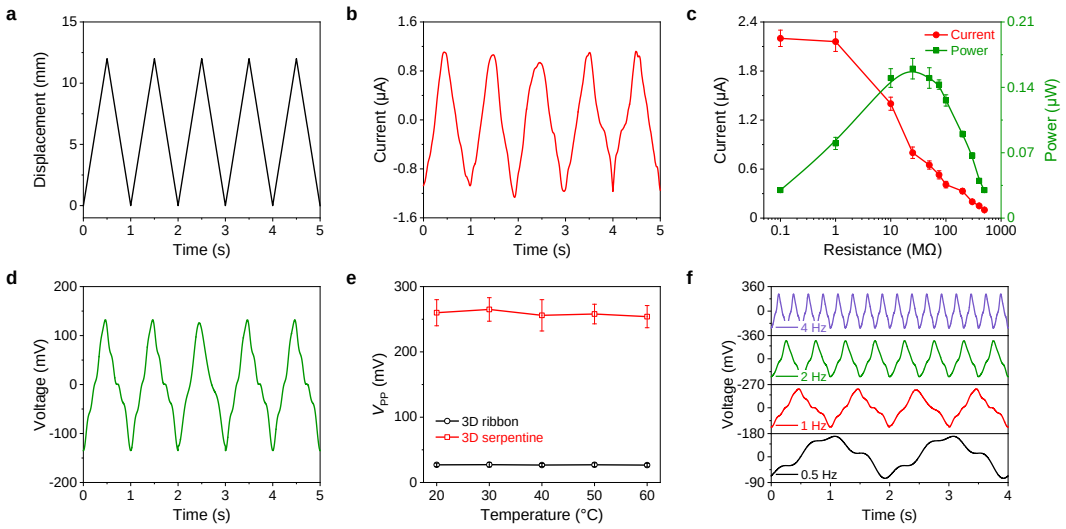

Figure S22. Output characterization of the 3D piezoelectric serpentine for energy harvesting. **a**) Real-time displacement of the magnet. **b**-**d**) Output **b**) current waveforms, **c**) peak current and corresponding maximum power at different external load resistances, and **d**) voltage waveforms of the 3D piezoelectric serpentine under the operating frequency of 1 Hz. Error bars are the standard error deviation from five measurements. **e**) Effect of temperature on output performance of the 3D piezoelectric serpentine under the operating frequency of 1 Hz. Error bars are the standard error deviation from five measurements. **f**) Time-domain output voltage of the 3D piezoelectric serpentine under different operating frequencies.

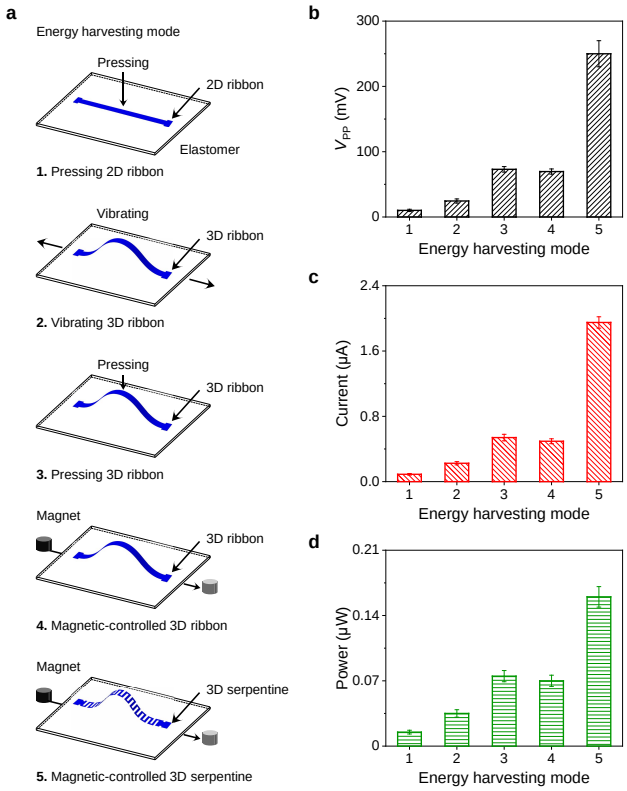

Figure S23. Comparison of output performance among different energy harvesting modes. **a**) Schematic illustration of different energy harvesting modes. **b**-**d**) Comparison of the **b**) V_{PP}, **c**) peak short-circuit current, and **d**) maximum power among different energy harvesting modes.

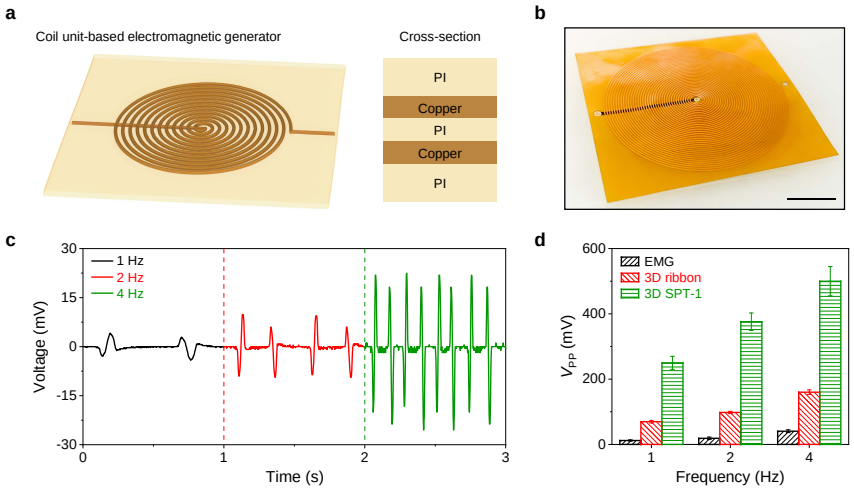

Figure S24. Output performance of the coil unit-based EMG. a) Schematic illustration of the coil unit-based EGM. **b**) Optical image of the Cu coil unit. Scale bar, 1 cm. **c**) The output voltage of EMG at different operating frequencies. **d**) The comparison of the frequency-domain output V_{PP} over the EMG, the 3D ribbon and 3D SPT-1.

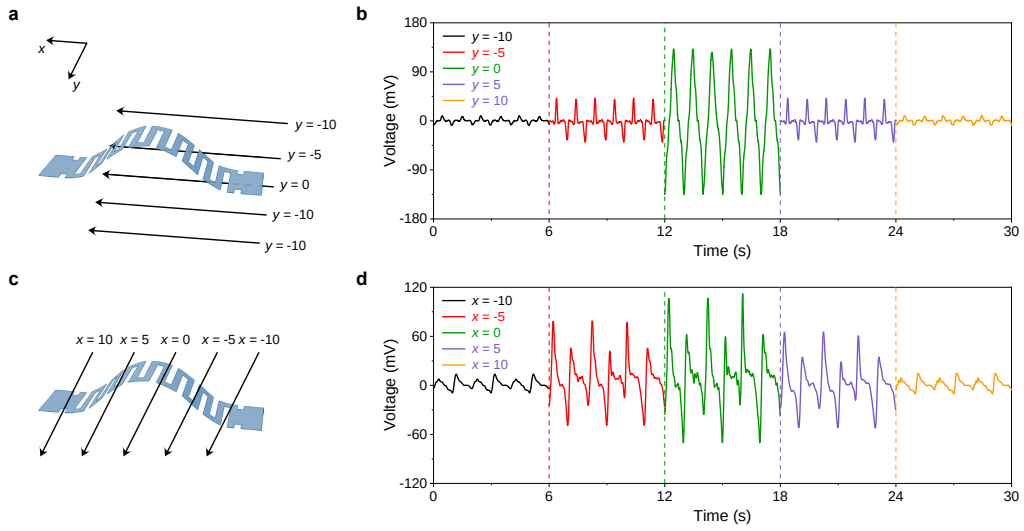

Figure S25. Output performance of the 3D piezoelectric serpentine along different directions. **a**,**b**) In-plane movement of magnet along the *x* axis with **a**) different longitudinal distance, and **b**) corresponding output performance at the operating frequency of 1 Hz. **c**,**d**) In-plane movement of magnet along the *y* axis with **c**) different lateral distance, and **d**) corresponding output performance at the operating frequency of 1 Hz.

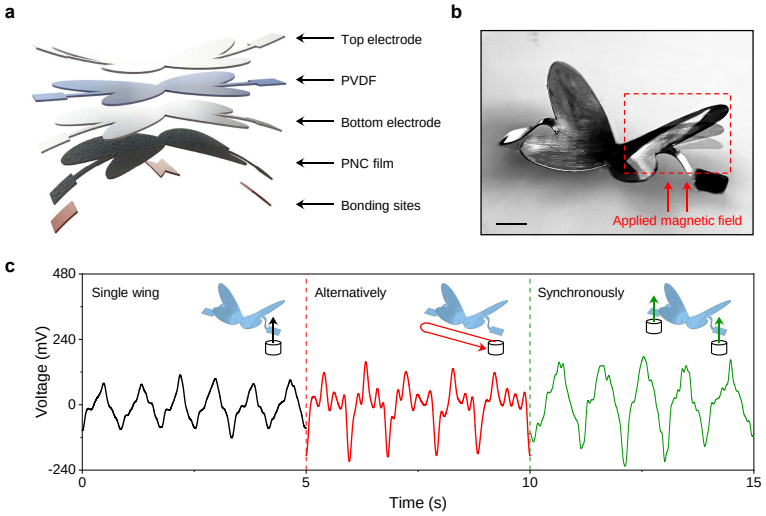

Figure S26. Output characterization of the 3D piezoelectric butterfly. a) Exploded schematic illustration of the piezoelectric butterfly. **b**) Superimposed optical image of the deformation of 3D piezoelectric butterfly under the applied magnetic field. Scale bar, 3 mm. **c**) Output voltage waveforms under different magnetic-controlled modes. Insets: illustration of the movements of magnets.

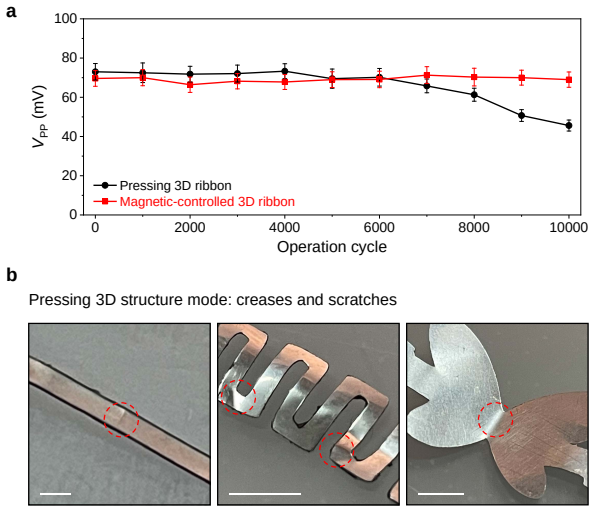

Figure S27. Long-term stability of the 3D structure under two different energy harvesting modes. a) Comparison of the V_{PP} of the 3D piezoelectric ribbon under two different modes during 10,000 operation cycles. **b**) Optical images of the damages on different 3D structures after long-term pressing. Scale bars, 4 mm.

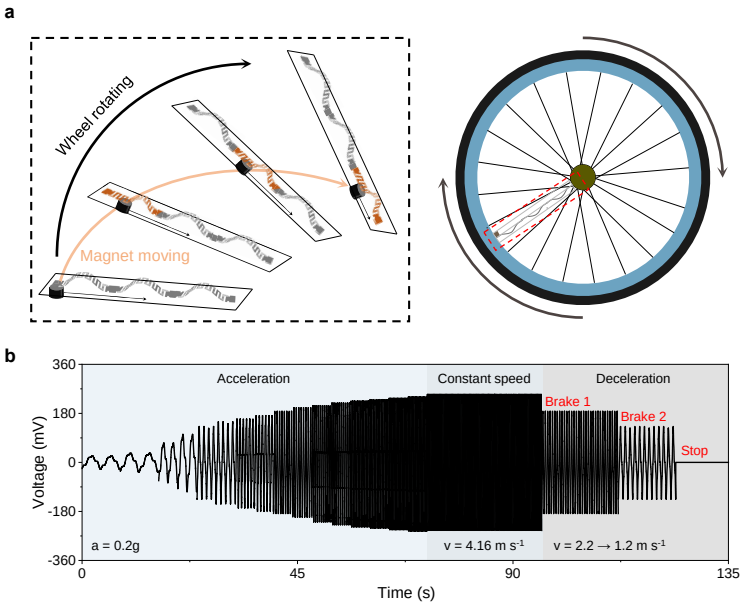

Figure S28. Application of the magnetic-controlled piezoelectric harvester based on 3D serpentine array as an active sensor for bicycle motion sensing. a) Schematic illustration of the 3D piezoelectric harvester cooperated with a bicycle wheel. **b**) Real-time output voltage during different operations of biking.

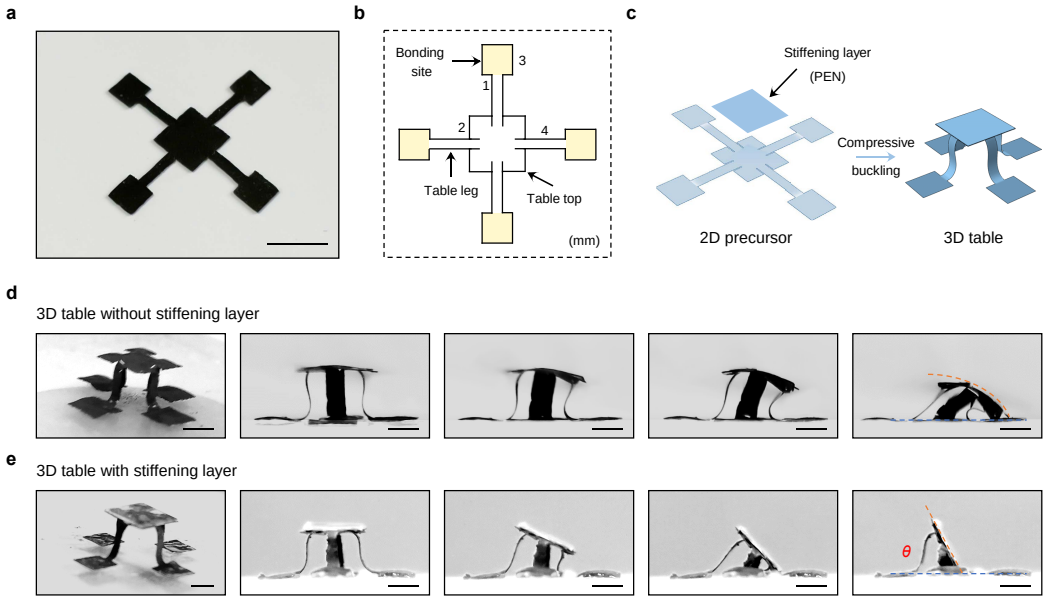

Figure S29. Characterization of the 3D table structure. a) Optical image of the 2D PNC precursor. Scale bar, 5 mm, **b**) Structural design and dimension parameters (unit: mm) of the 2D PNC precursor. **c**) Mechanical-guided compressive-bulking process for 3D table structure with PEN stiffening layer. **d**,**e**) Optical images of **d**) 3D table without stiffening layer and **e**) 3D table with the stiffening layer under different magnetic-controlled states. Scale bars, 3 mm.

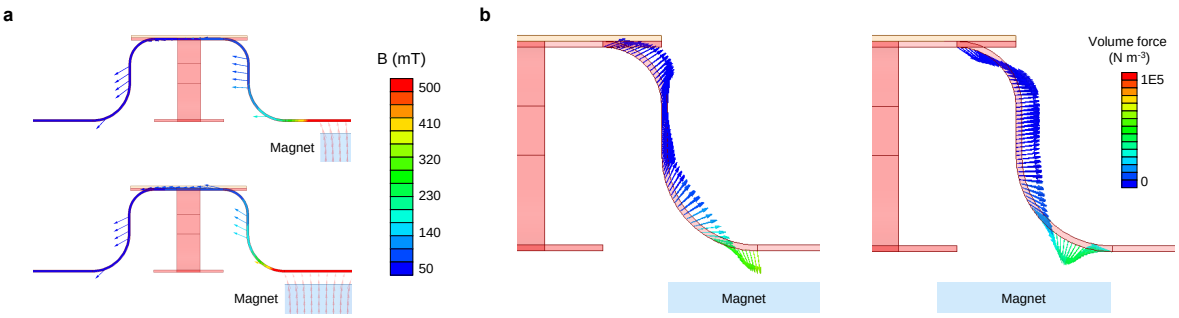

Figure S30. FEA results of the magnetic-controlled 3D table under different conditions of magnetization. a) Magnetization behavior. **b**) Volume force distribution.

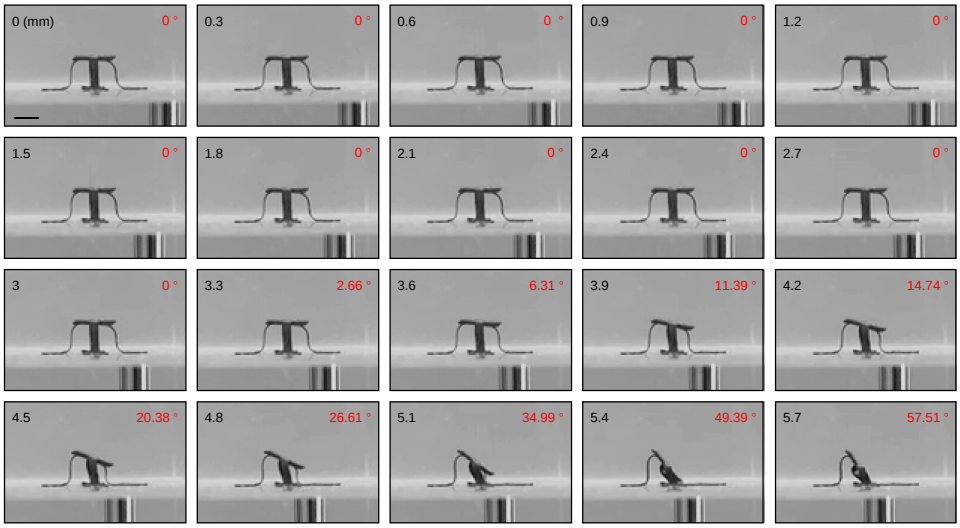

Figure S31. Optical images of the magnetic-controlled 3D table with precise control. Scale bar, 3 mm.

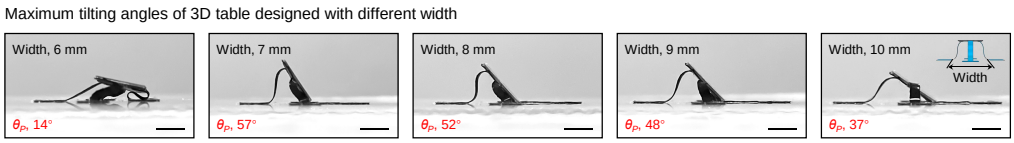

Figure S32. Optical images of 3D table (width: from 6 to 10 mm) under the maximum tilting angles. Scale bars, 3 mm.

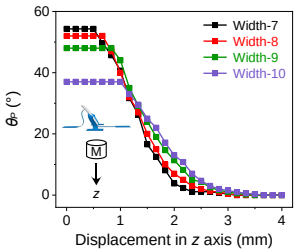

Figure S33. At the state with maximum tilting angle, the variation of the tilting performance with the increasing gap of the magnet along z axis for 3D table with different designed widths.

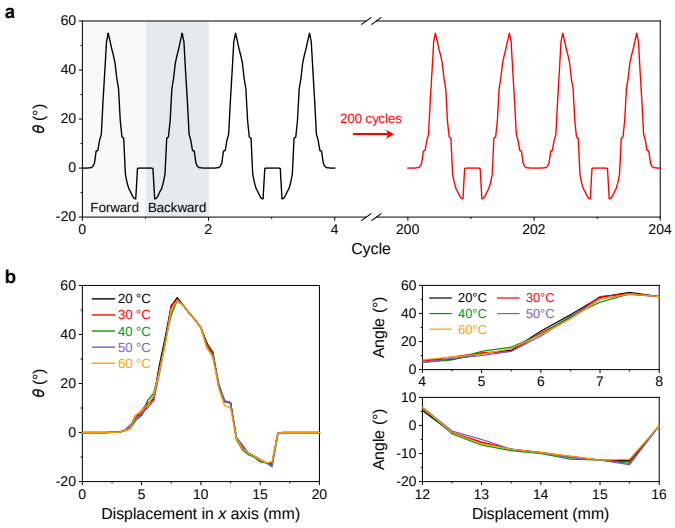

Figure S34. Stability evaluation of the magnetic-controlled 3D table. a) Mechanical stability of magnetic-controlled 3D table under the long-term periodic movement of the magnet. **b**) Effect of temperature on the stability of deformation of the magnetic-controlled 3D table.

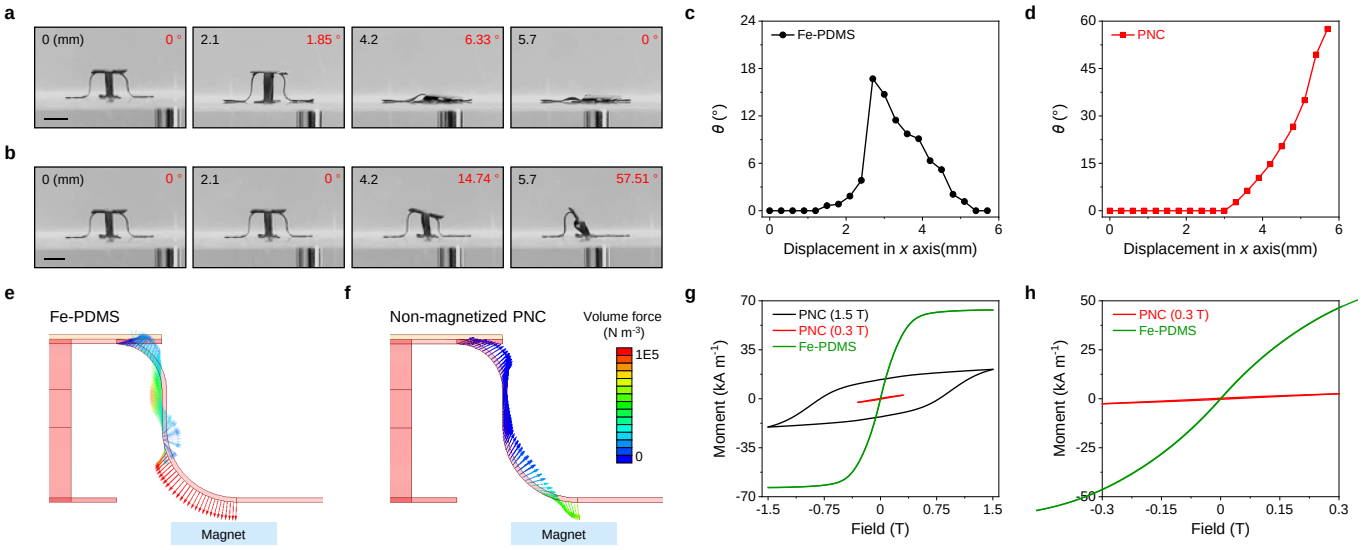

Figure S35. Comparison between Fe-PDMS-based and PNC-based 3D tables. a,**b**) The unidirectional tilting process of **a**) Fe-PDMS-based and **b**) PNC-based 3D tables with the movement of the external magnet. Scale bars, 3mm. **c**,**d**) The variation of tilting angle with the displacement of the magnet along *x* axis of **c**) Fe-PDMS-based and **d**) PNC-based 3D tables. **e**,**f**) FEA results of the **e**) Fe-PDMS-based and **f**) PNC-based 3D tables with the approach of the external magnet. **g**,**h**) Static magnetic hysteresis loops of Fe-PDMS and PNC under the magnetic field of **g**) 1.5 T and **h**) 0.3 T.

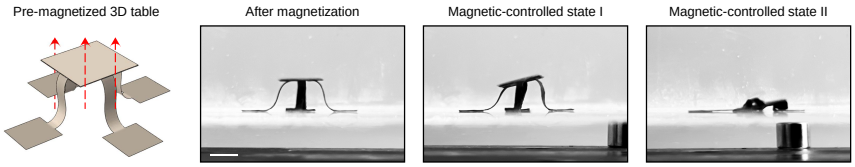

Figure S36. Schematic illustration and optical images of the magnetic controlled states of the 3D table with pre-magnetized process. Scale bar, 3 mm.

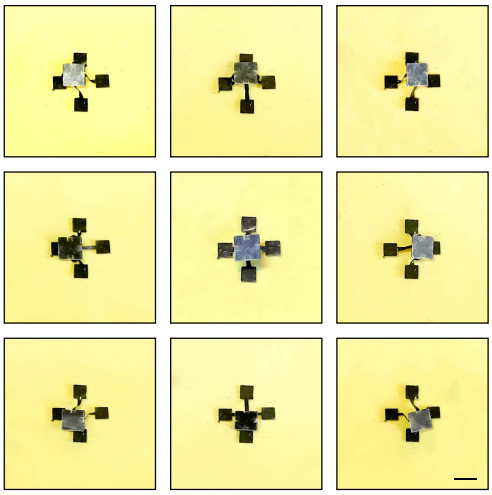

Figure S37. Optical images showing the omnidirectional rotation of the magnetic-controlled 3D table (top view). Scale bar, 5 mm.

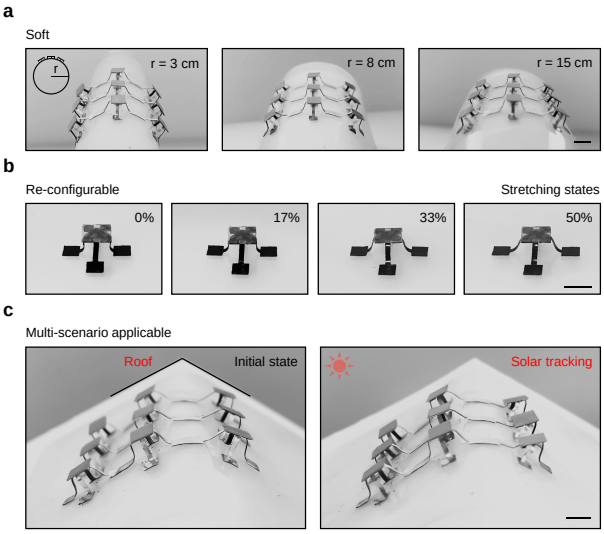

Figure S38. Demonstration of the 3D table array with different features. a-c) The appealing features of the 3D table array, including **a**) soft, **b**) re-configurable, and **c**) multi-scenario applicable. Scale bars, 5 mm.

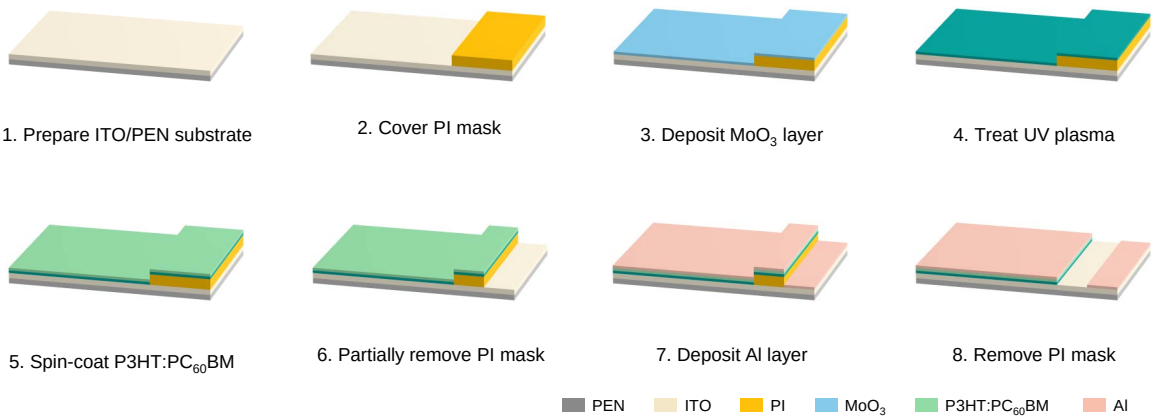

Figure S39. Fabrication process of the OSC.

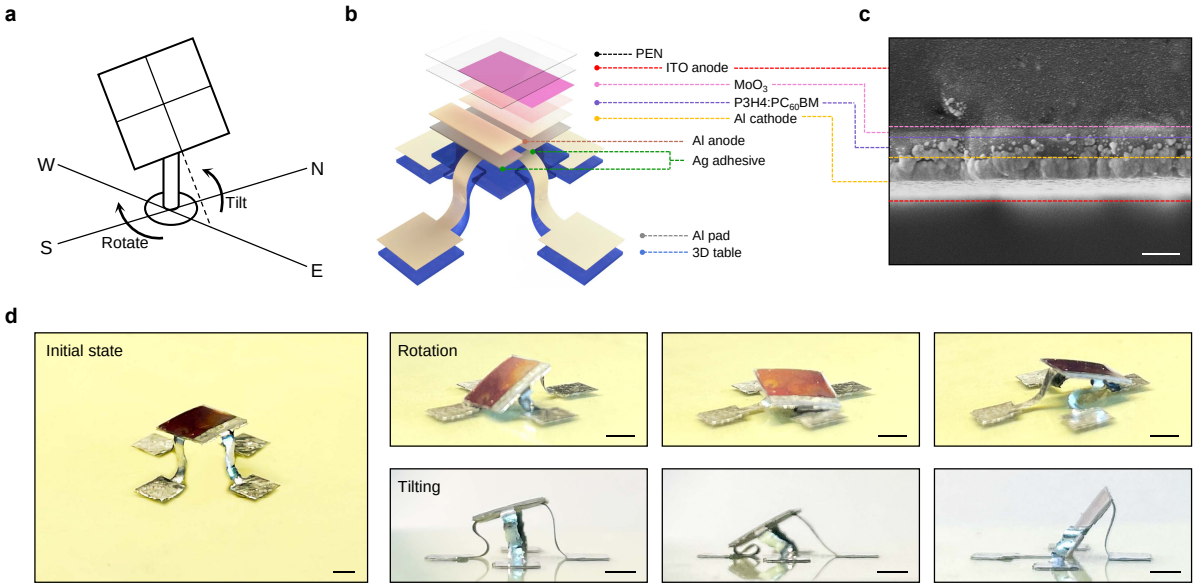

Figure S40. Demonstration of 3D table-based solar tracking systems. a) Traditional dual-axis solar tracking system with complex electro-mechanical module. **b**) Schematic illustration of the 3D table-based solar tracking system. **c**) SEM image (cross-section view) of the prepared OSC. Scale bar, 200 nm. **d**) Optical images of the 3D table-based solar tracking system with two magnetic-controlled working modes: omnidirectional rotation and unidirectional tilting. Scale bars, 2 mm.

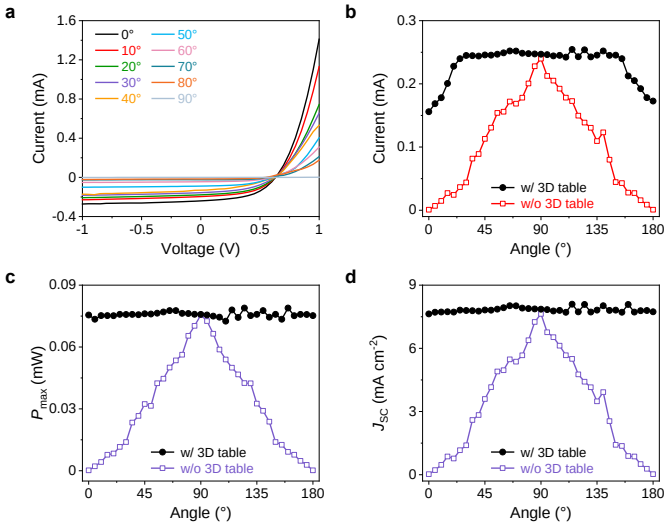

Figure S41. Enhanced output of the OSC integrated with 3D robotic structure. a) Current-voltage (*I*-*V*) curves of the OSC under different incident angles. **b**-**d**) Comparison of **b**) output current, **c**) real-time peak power (P_{max}), and **d**) current density (J_{SC}) between the 3D table-based solar tracking system and single OSC under different incident angles.

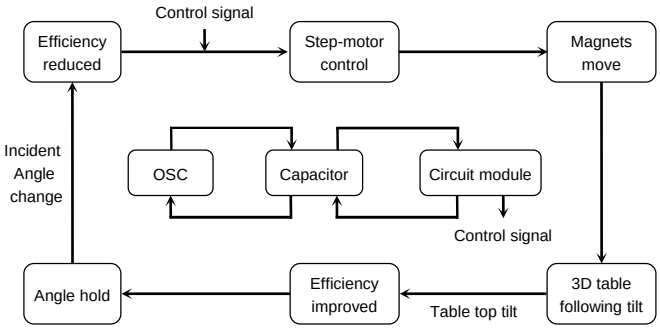

Figure S42. Block diagram of the magnetic-controlled solar tracking system.

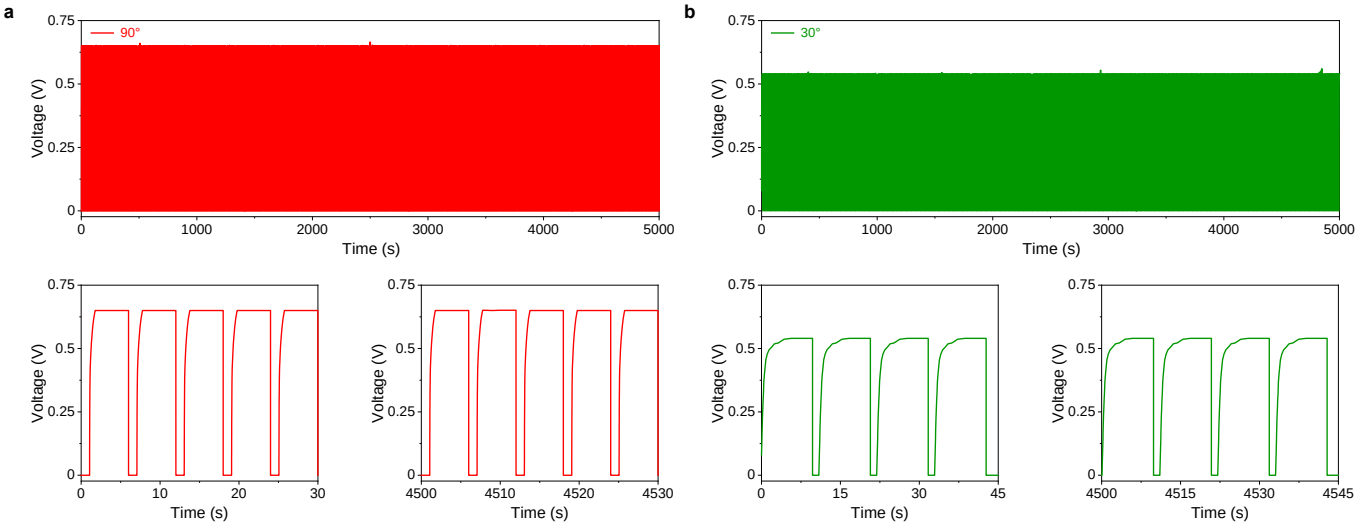

Figure S43. Cyclic charging capability of the OSC. a,**b**) The cyclic charging-discharging curves of a capacitor (22 μF) charged by the OSC under the incident angles of **a**) 90º and **b**) 30º. Top frames in (**a**) and (**b**): long-term tests with durations of 5,000 s. Bottom frames in (**a**) and (**b**): zoomed-in curves at the first and last few cycles.

Table S1. Detailed testing parameters for the magnetic hysteresis loop.

Parameter	Value	Unit
Field range	3 E3	Gs
Moment range	5 E-2	Gs
Averaging time	1 E-1	s
Temperature	25	°C
Gradient	2	/
Probe factor	6.36 E-2	/
Probe Q	2.24 E1	/
Probe resonance	6.49 E2	Hz
Operating frequency	6.49 E2	Hz